Quantitative comparison using Generalized Relative Object Detectability (G-ROD) metrics of an amorphous selenium detector with high resolution Microangiographic Fluoroscopes (MAF) and standard flat panel detectors (FPD)

M. Russ[a], **A. Shankar**[a], **A. Jain**[a], **S. V. Setlur Nagesh**[a], **C. N. Ionita**[a], **C. Scott**[b], **K. S. Karim**[b], **D. R. Bednarek**[a], and **S. Rudin**[a]

[a]Toshiba Stroke and Vascular Research Center, University at Buffalo, Buffalo, NY

[b]Electrical and Computer Engineering, University of Waterloo, Waterloo, ON

Abstract

A novel amorphous selenium (a-Se) direct detector with CMOS readout has been designed, and relative detector performance investigated. The detector features include a 25μm pixel pitch, and 1000μm thick a-Se layer operating at 10V/μm bias field. A simulated detector DQE was determined, and used in comparative calculations of the Relative Object Detectability (ROD) family of prewhitening matched-filter (PWMF) observer and non-prewhitening matched filter (NPWMF) observer model metrics to gauge a-Se detector performance against existing high resolution micro-angiographic fluoroscopic (MAF) detectors and a standard flat panel detector (FPD). The PWMF-ROD or ROD metric compares two x-ray imaging detectors in their relative abilities in imaging a given object by taking the integral over spatial frequencies of the Fourier transform of the detector DQE weighted by an object function, divided by the comparable integral for a different detector. The generalized-ROD (G-ROD) metric incorporates clinically relevant parameters (focal-spot size, magnification, and scatter) to show the degradation in imaging performance for detectors that are part of an imaging chain. Preliminary ROD calculations using simulated spheres as the object predicted superior imaging performance by the a-Se detector as compared to existing detectors. New PWMF-G-ROD and NPWMF-G-ROD results still indicate better performance by the a-Se detector in an imaging chain over all sphere sizes for various focal spot sizes and magnifications, although a-Se performance advantages were degraded by focal spot blurring. Nevertheless, the a-Se technology has great potential to provide breakthrough abilities such as visualization of fine details including of neuro-vascular perforator vessels and of small vascular devices.

Keywords

Comparative metrics; amorphous selenium; CMOS; micro-angiography; relative object detectability; generalized metrics; DQE

INTRODUCTION

It is well documented that visualization of fine detail using x-ray imaging is paramount for performing successful endovascular image-guided interventional procedures[1]. Current flat panel detector technology provides pixel sizes on the order of 200 microns, falling short of the resolution necessary to accurately resolve vascular device detail. A novel amorphous selenium (a-Se) detector has been proposed[2,3] that will have incomparably high resolution if achieved. The new detector will feature 25 μm pixel size, 1000 μm active a-Se layer, and a 10 V/μm bias field. The a-Se detector will have CMOS readout electronics, eliminating the electronic noise issues that historically plagued a-Se TFT detectors. The expected modulation transfer function (MTF) for this detector was prospectively calculated using these expected detector characteristics and physical phenomena including primary photoelectron range, re-absorption of k-fluorescence and Compton scattered photons, and charge carrier trapping given by the Hecht relation. The MTF for the a-Se detector was used to calculate the DQE, using a white noise spectrum associated with the electronic noise of the CMOS readout.

In order to get a comprehensive comparison of the proposed detector to existing high resolution micro-angiographic fluoroscopic (MAF) detectors, the Relative Object Detectability (ROD) family of metrics was employed. The ROD metrics provide a quantitative, task-specific comparison of detector performance using the geometry of the object being imaged and intrinsic detector abilities given by the DQE. Using the generalized-DQE (GDQE), the ROD metrics can include the phenomena that degrade detector performance once a detector becomes part of an imaging chain, including geometric unsharpness, focal spot blurring, and scatter blur. Previously, the ROD metrics utilized the ideal observer model to compare detectors purely on the basis of their abilities. The ROD family of metrics has now been expanded to include the imperfect human perspective of the non-prewhitened human observer model.

MATERIALS AND METHODS

In order to perform prospective evaluation of the new a-Se detector, the detector MTF was calculated using the proposed specifications indicated above. Using these characteristics and other physical blurring phenomena, a point spread function was calculated and the Fourier transform was taken to obtain the detector MTF[2], as shown in Figure 1. Using an electronic noise level of 300 electrons rms, the DQE was calculated for ROD analysis[2,3].

The previously presented ROD metric[4,5,6] that utilizes the ideal observer model is defined as the integral over spatial frequencies of the Fourier transform of an object function weighted by the detector DQE for one detector, then divided by the comparable integral for another detector, as shown in Equation 1.

$$ROD = \frac{\int\int |OBJ(u,v)|^2 DQE_1(u,v)\,du\,dv}{\int\int |OBJ(u,v)|^2 DQE_2(u,v)\,du\,dv} \quad \text{EQ1}$$

The object function is defined as the position-dependent difference in signal relative to background for an object in air, and the task-specific frequency spectrum is generated by taking the Fourier Transform of the object function as can be seen in Equations 2 and 3

$$OBJ(x,y) = \frac{background - signal}{background} = \frac{N_0 - N_0 e^{-\mu t(x,t)}}{N_0} = 1 - e^{-\mu t(x,y)}$$ EQ2

$$OBJ(u,v) = \iint obj(x,y) e^{-2\pi i(ux+vy)} \, dx dy$$ EQ3

where obj(x,y) is defining the object function in real space, N_0 is the incident number of photons, μ is the attenuation coefficient, t(x,y) is a function describing the thickness of the object, and OBJ(u,v) is the Fourier transformed function of obj(x,y). The ROD is capable of giving a quantitative comparison of relative detector performances in imaging a specific object, the result of which depends primarily on the detector DQE and the object geometry. The detector DQEs used for these calculations are presented in Figure 2. The DQE of the a-Se detector simulated using 50 keV photons is superior for all spatial frequencies as compared to the measured DQEs for the other detectors for which an RQA5 spectrum was used for their measurement. A mono-energetic x-ray beam is not currently plausible for real time x-ray imaging, so a calculation of the predicted quantum detective efficiency (QDE) was performed for the a-Se detector using an RQA5 bremsstrahlung spectrum. This calculated QDE was determined to be 0.905, higher than the mono-energetic QDE of 0.84.

To incorporate clinically relevant parameters, including focal spot blur, magnification, and scatter, the PWMF G-ROD metric, or G-ROD[7], is defined in the following way:

$$G-ROD(\rho, X, m) = \frac{\iint |OBJ(u,v)|^2 GDQE_1(u,v,\rho,X,m) \, du dv}{\iint |OBJ(u,v)|^2 GDQE_2(u,v,\rho,X,m) \, du dv}$$ EQ4

The G-ROD uses the GDQE[8,9] metric instead of the detector DQE to compare detectors that are part of an imaging chain, which is defined in Equation 5

$$GDQE(u, \rho, X, m) = \frac{GMTF(u, \rho, m)^2}{m^2 \phi_{in} GNNPS(u, X, m)}$$ EQ5

where the GMTF, or the generalized modulation transfer function is defined as

$$GMTF(u, \rho, m) = \left[(1-\rho) MTF_f \left(\frac{m-1}{m} u \right) + \rho MTF_s \left(\frac{u}{m} \right) \right] MTF_d \left(\frac{u}{m} \right).$$ EQ6

Here the MTF_f is the focal spot blur MTF, MTF_s is the scatter blur MTF, MTF_D is the detector MTF, u is spatial frequency, ϕ_{in} is the x-ray fluence incident on the detector face, ρ is the scatter fraction, X is exposure, and m is the magnification of the plane of the object. The generalized normalized noise power spectrum (GNNPS) is simply the NNPS divided by the square of the magnification.

The NPWMF ROD metric, or ROD_{NP}, uses a sub-optimal human observer model that, while it includes all information from the image, does not properly treat correlated noise, and has less than ideal performance for images containing frequency dependent noise[10]. This is similar to human observer performance in that humans cannot prewhiten correlated noise in an image. The model for calculating the non-prewhitened signal to noise ratio (SNR^2_{NP}) is defined below in Equation 7. To use this as a comparative metric the SNR^2_{NP} is calculated for a given detector, and, as is done with the ROD metric, the ratio of two comparable integrals is taken to determine the relative performance of a pair of detectors.

$$SNR^2_{NP} = \frac{\left[\int\int |OBJ(u,v)|^2 MTF_1(u,v)^2 \, du \, dv \right]^2}{\int\int |OBJ(u,v)|^2 MTF_1(u,v)^2 NPS_1(u,v) \, du \, dv} \quad \text{EQ7}$$

The ROD_{NP} metric requires an explicitly defined noise power spectrum, but without the a-Se detector, measurement of the NPS was not possible. The NPS for the a-Se detector was then calculated using the noise response method[11,12].

Using the ROD and G-ROD metrics for the ideal observer, and the ROD_{NP} models, the performance of the amorphous selenium detector was compared to that of the MAF-CCD, MAF-CMOS, and FPD detectors in imaging mathematically modeled aluminum spheres of varying diameter (d = 0.05–0.6mm). The MAF-CCD and MAF-CMOS are high resolution indirect detectors that utilize a CsI(Tl) phosphor of 500μm and 600μm, respectively, for x-ray detection[13,14,15]. The MAF-CCD detector uses a CCD camera with 12μm pixel size coupled to a fiber optic taper with a 2.88:1 ratio, giving an effective pixel size of 35μm and effective circular field of view 3.6cm in diameter. The MAF-CCD detector features a light image intensifier (LII), providing high dynamic range for imaging well at fluoroscopic and angiographic exposure levels. The MAF-CMOS detector utilizes a CMOS readout with 75μm pixel pitch, and has a rectangular 12cm × 7cm field of view. The flat panel detector uses a 600μm CsI(Tl) phosphor, and a TFT readout with 194μm pixel size. Diagrams of the MAF detectors are shown in Figure 3.

RESULTS

ROD calculations indicated vastly superior performance by the a-Se detector in imaging small aluminum spheres, especially for the smaller spheres[16]. For the ideal observer, calculations for the 50μm diameter sphere indicated the a-Se detector's ability was 7.3 times greater than that of the MAF-CCD and 9.3 times greater than that of the MAF-CMOS (see Fig. 4). The a-Se performance was 58 times greater than that of the standard FPD for the

smallest spheres (see plots on the left in Fig. 4). Low frequency performance was comparable for all detector pairs and dictated by each detector's QDE value. The existing MAF detectors were also compared to the FPD and each other using the ROD metrics, comparing their relative performance for the same spheres mentioned above. The MAF-CCD and MAF-CMOS both exhibit superior performance over the FPD for the smaller spheres, and show comparable performance for the largest spheres.

The G-ROD results are presented separately to better show performance variation due to focal spot blurring, so the small focal spot calculations are shown in Fig. 5, medium focal spot results in Fig. 6, and large focal spot size results in Fig 7. Detector performance was calculated for two different levels of magnification (M=1.05,1.2) at each focal spot size (0.3mm, 0.5mm, and 0.8mm). It is clear that while the amorphous selenium detector exhibits superior performance, especially over the FPD, for all simulated cases, the advantage it holds over the existing MAF detectors is somewhat diminished once the detector experiences high magnification and greater focal spot blurring due to increased focal spot size. The simulated a-Se GMTFs for various clinical imaging conditions are plotted in Figure 8 to show the degradation of the MTF over all frequencies.

The non-prewhitened observer ROD results, as shown in Figure 9, seem to indicate that a human observer would detect the aluminum spheres more easily if looking at an image taken by the amorphous selenium detector as compared to the other MAF and FPD detectors. The quantitative advantage of the a-Se detector with respect to the other detectors in imaging the smallest spheres is given by the respective calculated NPWMF ROD values; the a-Se performed better by a factor of 21 greater than the MAF-CMOS, 33 times greater than the MAF-CCD, and 87 times greater than the FPD. Aside from the increase in ROD_{NP} value, the trends exhibited over all sphere sizes are comparable to those observed in the ROD results.

DISCUSSION

It is clear from the ROD results and the a-Se GMTFs that the advantage of the high resolution of the a-Se detector is lost when the finite size of the focal spot is considered. Should the a-Se detector be built, a smaller focal spot size would be necessary for the detector to reach its full potential. The detector should also be used under minimal magnification to prevent geometric unsharpness, which, as seen in the GMTF plots, can be crippling for high frequency performance. The large MTF values at the high frequencies may indicate the possibility for noise aliasing to occur. Inclusion of the apodized aperture[17], or another method of mitigating noise aliasing may be necessary for future use of the a-Se detector.

The prospectively calculated detector MTF describes the performance of the detector without any methods in place to mitigate the deleterious effects of charge carrier trapping. Image lag and ghosting have historically caused varying levels of reduced image quality when electrons traversing the a-Se are trapped in the bulk[18,19]. Several methods to diminish the trapping of charge carriers are being investigated for this design, including organic blocking layers.[20,21,22]

The non-prewhitened observer model indicates the degradation of detectability due to frequency-dependency in the image noise. When comparing the results of the ROD calculation to those of the ROD_{NP} calculations for the same spheres, it seems that the relative performance of the a-Se is greater despite the use of the human observer model. However, this increase in relative performance is due to the fact that the NPS calculated for the a-Se detector using the noise response method had very little noise correlation, and was almost white noise, meaning the existing MAF and FPD detectors experienced degradation in the ROD_{NP} calculation that the a-Se detector did not. Future calculations using the ROD_{NP} metric will be attempted once the detector is built and a noise power spectrum can be measured.

CONCLUSIONS

The a-Se with CMOS readout is unique and appears to have distinctive advantages of incomparable high resolution, low noise, and expandable design. The a-Se direct detection system will be a powerful imaging tool in angiography, with potential break-through applications in diagnosis and treatment of neuro-vascular disease where visualization of small vessels and interventional device detail can be crucial.

Acknowledgments

References

1. Rudin S, Bendarek DR, Hoffman KR. Endovascular image-guided interventions (EIGIs). Med Phys. 2008; 35:301–309. [PubMed: 18293585]

2. Scott, CC., Allec, N., Karim, KS. A study of factors limiting spatial resolution using a 25 micron pixel pitch direct-detection amorphous selenium imaging system. Proc. SPIE Medical Imaging 2012: Physics of Medical Imaging 8313; 2012;

3. Scott, CC., Abbaszadeh, S., Ghanbarzadeh, S., Allan, G., Farrier, M., Cunningham, IA., Karim, KS. Amorphous selenium direct detection CMOS digital x-ray imager with 25 micron pixel pitch. Proc. SPIE Medical Imaging 2014: Physics of Medical Imaging 9033; 2014;

4. Russ, M., Singh, V., Loughran, B., Bednarek, DR., Rudin, S. New Family of Generalized Metrics for Comparative Imaging System Evaluation. Proc. SPIE Medical Imaging 2015: Physics of Medical Imaging 9412; 2015;

5. Singh, V., Jain, A., Bednarek, DR., Rudin, S. Relative object detectability (ROD): a new metric for comparing x-ray image detector performance for a specified object of interest. Proc SPIE Int Soc Opt Eng. 9033; 2014;

6. Russ M, Ionita C, Bednarek DR, Rudin S. Quantitative Comparison of a High Resolution Micro-Angiographic Fluoroscopic (MAF) Detector with a Standard Flat Panel Detector (FPD) Using the New Metric of Generalized Measured Relative Object Detectability (GM-ROD). Med Phys. 2015; 42:3217.

7. Singh V, Jain A, Bednarek DR, Rudin S. Generalized Relative Object Detectabilty (G-ROD): A Metric for Comparing X-ray Imaging Detector Systems. Med Phys. 2014; 41:136.

8. Kyprianou IS, Rudin S, Bednarek DR, Hoffman K. Generalizing the MTF and DQE to include x-ray scatter and focal spot unsharpness: application to a new microangiographic system. Med Phys. 2005; 32:613–26. [PubMed: 15789608]

9. Kyprianou IS, Rudin S, Bednarek DR, Hoffman K. Study of the Generalized MTF and DQE for a New Microangiographic System. Proc SPIE Int Soc Opt Eng. 2004; 5368:349–360. [PubMed: 21603129]

10. ICRU Report No.54. International Commission on Radiation Units and Measurements; Bethesda, MD: 1996. Medical Imaging- The Assessment of Image Quality.

11. Kuhls-Gilchrist A, Jain A, Bednarek DR, Hoffman KR, Rudin S. Accurate MTF measurement in digital radiology using noise response. Med Phys. 2010; 37:724–735. [PubMed: 20229882]

12. Zhao W, Rowlands JA. Digital radiology using active matrix readout of amorphous selenium: Theoretical anlaysis of detective quantum efficiency. Med Phys. 1997; 24:1819–1833. [PubMed: 9434965]

13. Jain A, Bednarek DR, Ionita CN, Rudin S. A theoretical and experimental evaluation of the microangiographic fluoroscope: A high-resolution region-of-interest x-ray imager. Med Phys. 2011; 38(7):4112–4126. [PubMed: 21859012]

14. Loughran, B., Vasan, SNS., Singh, V., Ionita, CN., Jain, A., Bednarek, DR., Titus, A., Rudin, S. Design Considerations for a new, high resolution Micro-Angiographic Fluoroscope based on a CMOS sensor (MAF-CMOS). Proc. SPIE Medical Imaging 2013: Physics of Medical Imaging 8668; 2013;

15. Jain, A., Bednarek, DR., Rudin, S. Experimental and theoretical performance analysis for a CMOS-based high resolution image detector. Proc. SPIE Medical Imaging 2014: Physics of Medical Imaging 9033; 2014;

16. Russ M, Setlur Nagesh SV, Ionita CN, Scott C, Karim KS, Bednarek DR, Rudin S. Relative Object Detectability Evaluation of a New High Resolution a-Se Direct Detection System Compared to Indirect Micro-Angiographic Fluoroscopic (MAF) Detectors. Med Phys. 2015; 42:3694.

17. Ismailova, E., Karim, KS., Cunningham, IA. Apodized-Aperture Pixel Design to Increase High-Frequency DQE and Reduce Noise Aliasing in X-Ray Detectors. Proc. SPIE Medical Imaging 2015: Physics of Medical Imaging 9412; 2015.

18. Zhao W, DeCresenzo G, Rowlands JA. Investigation of lag and ghosting in a-Se flat-panel detectors. Proc SPIE. 2002; 4682:9–20.

19. Zahangir Kabir M, Kasap SO. Modulation transfer function of photoconductive x-ray image detectors: effects of charge carrier trapping. J Phys D: Appl Phys. 2003; 36:2352.

20. Mahmood SA, Kabir MZ, Tousignant O, Greenspan J. Investigation of Ghosting Recovery Mechanisms in Selenium X-ray Detector Structures for Mammography. IEEE Transactions on Nuclear Science. 2012; 59

21. Abbaszadeh, S., Du, Z., Allec, N., Karim, KS. Application of organic semiconductors in amorphous selenium based photodetectors for high performance x-ray imaging. Proc. SPIE Medical Imaging 2013: Physics of Medical Imaging 8668; 2013;

22. Abbaszadeh S, Scott CC, Bubon O, Reznik A, Karim KS. Enhanced Detection Efficiency of Direct Conversion X-Ray Detector Using Polyimide as Hole-Blocking Layer. Scientific Reports. 2013
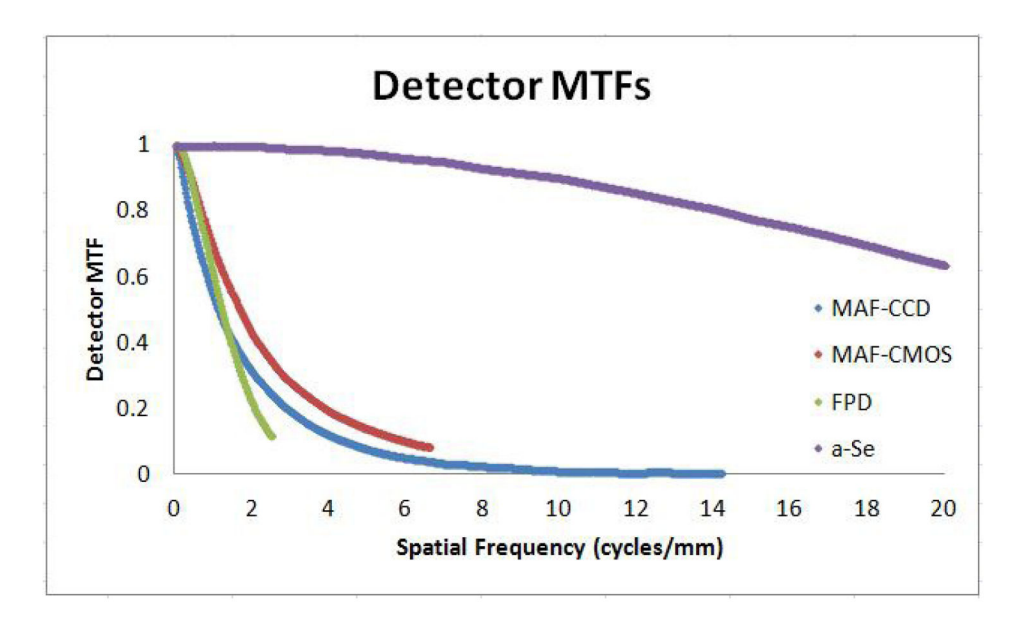
Figure 1.
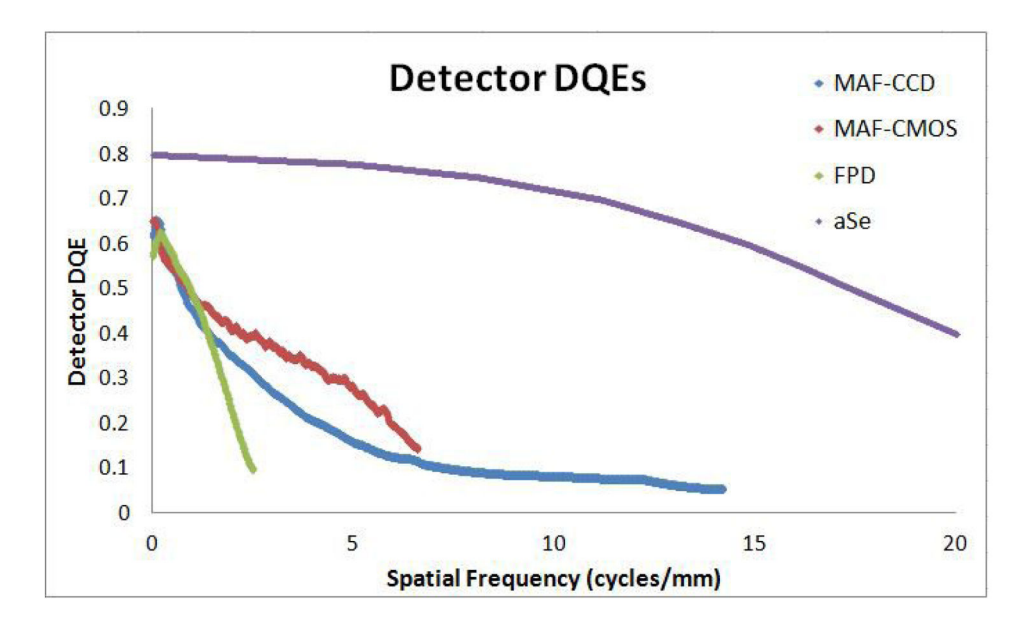The MTFs plotted for the a-Se detector and the existing MAF and FPD detectors.

Figure 2.
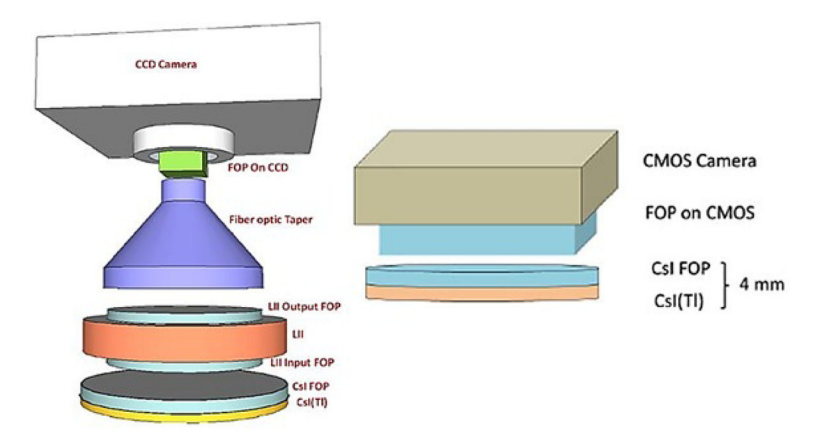The DQEs for the a-Se, MAF, and FPD detectors.

Figure 3.
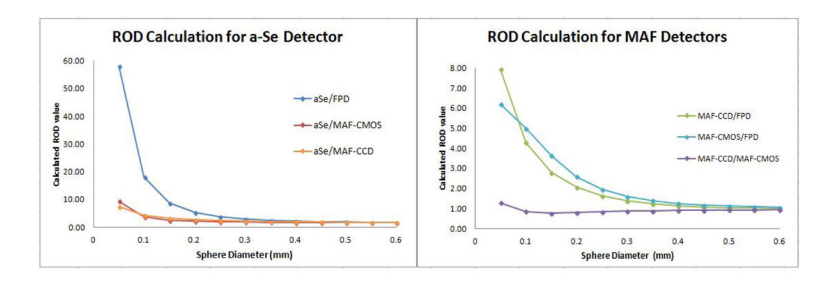Diagrams of the MAF-CCD (left) and MAF-CMOS (right).

Figure 4.
Results of ROD calculations comparing the new a-Se detector to the existing MAF and FPD detectors (left) and the results comparing the relative abilities of the existing detectors (right).
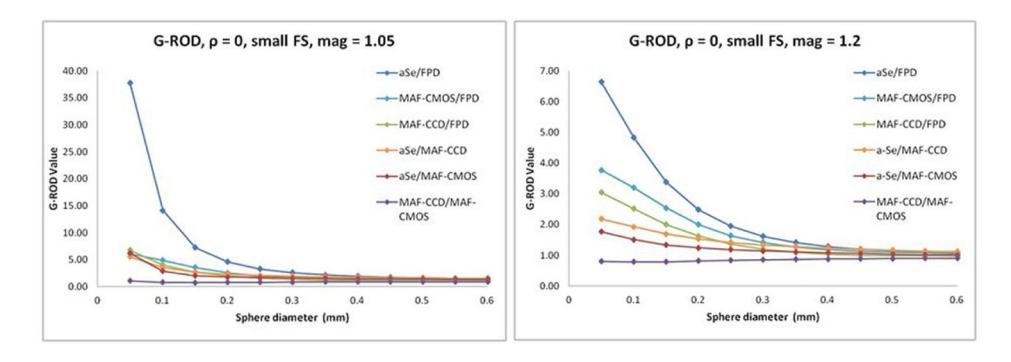
Figure 5.
G-ROD calculation results for small focal spot size, note the change in scale.
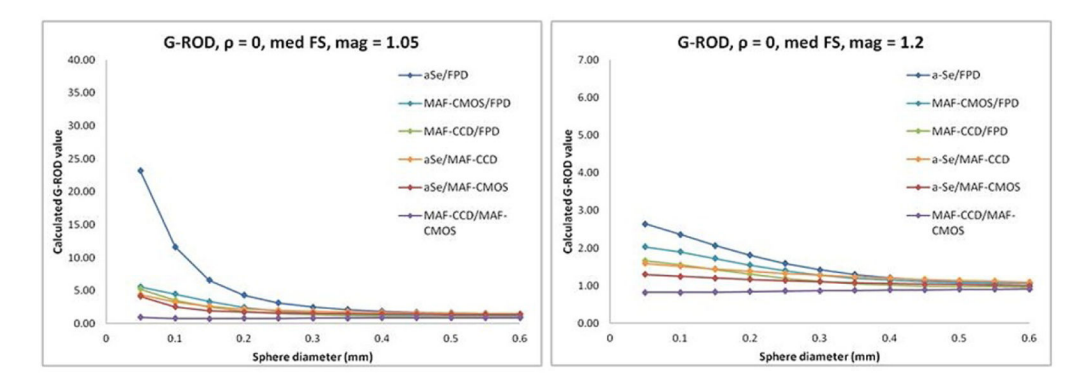
Figure 6.
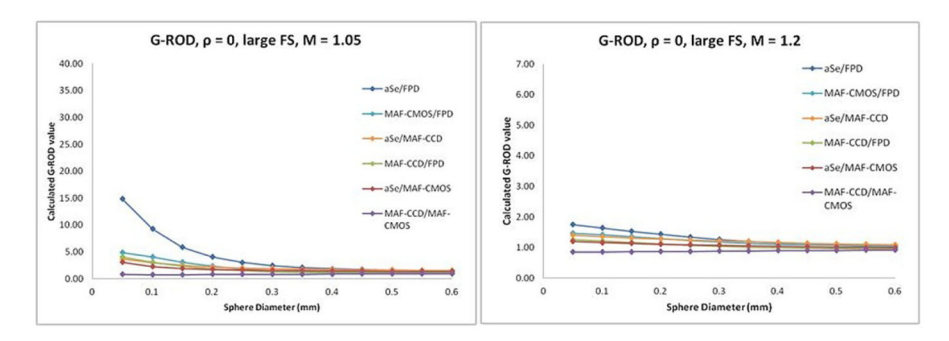G-ROD calculation results for medium focal spot size, note the change in scale.

Figure 7.
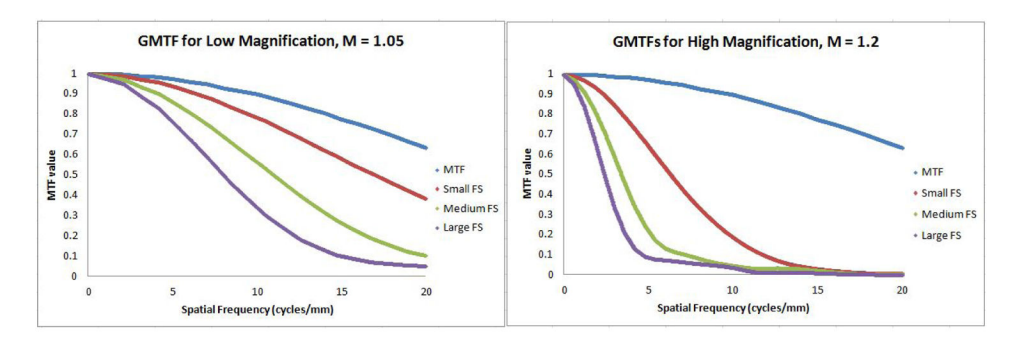G-ROD calculation results for large focal spot, note the change in scale.

Figure 8.
The results of GMTF calculations. The detector MTF is diminished, particularly at higher spatial frequencies, when the detriments due to focal spot blurring and geometric unsharpness are included.
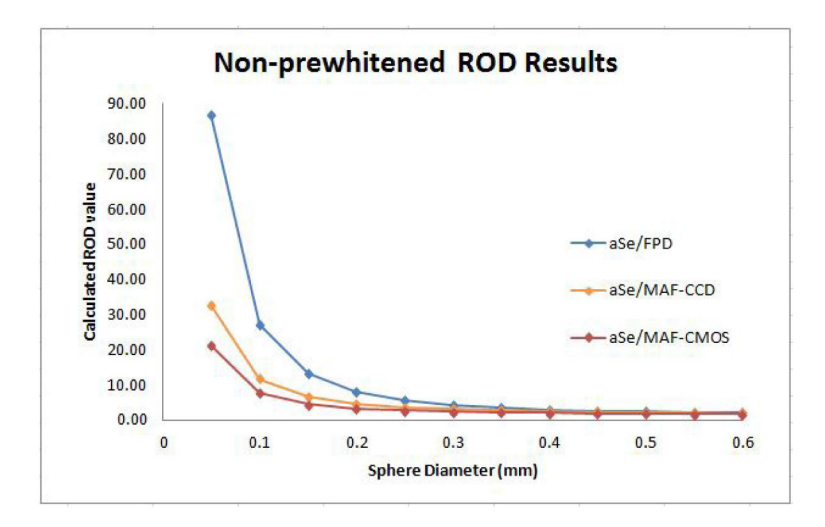
Figure 9.
The results of the non-prewhitened ROD calculations comparing the a-Se detector to the existing detectors.